www.acsnano.org

Dynamic Reconfiguration of Compressed 2D Nanoparticle Monolayers Paul Y. Kim, Yige Gao, Zachary Fink, Alexander E. Ribbe, David A. Hoagland,* and Thomas P. Russell*



Downloaded via UNIV OF MASSACHUSETTS AMHERST on November 3, 2022 at 14:52:07 (UTC). See https://pubs.acs.org/sharingguidelines for options on how to legitimately share published articles.

Cite This: ACS Nano 2022, 16, 5496-5506



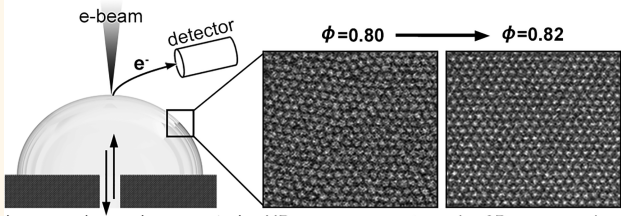
ACCESS

Metrics & More

Article Recommendations

Supporting Information

ABSTRACT: A Gibbs monolayer of jammed, or nearly jammed, spherical nanoparticles was imaged at a liquid surface in real time by in-situ scanning electron microscopy performed at the singleparticle level. At nanoparticle areal fractions above that for the onset of two-dimensional crystallization, structural reorganizations of the mobile polymer-coated particles were visualized after a stepwise areal compression. When the compression was small, slow shearing near dislocations and reconfigured nanoparticle bonding were observed at crystal grain boundaries. At larger



in vacuo drop volume control NP rearrangements under 2D compression

scales, domains grew as they rotated into registry by correlated but highly intermittent motions. Simultaneously, the areal density in the middle of the monolayer increased. When the compression was large, the jammed monolayers exhibited out-ofplane deformations such as wrinkles and bumps. Due to their large interfacial binding energy, few (if any) of the twodimensionally mobile nanoparticles returned to the liquid subphase. Compressed long enough (several hours or more), monolayers transformed into solid nanoparticle films, as evidenced by their cracking and localized rupturing upon subsequent areal expansion. These observations provide mechanistic insights into the dynamics of a simple model system that undergoes jamming/unjamming in response to mechanical stress.

KEYWORDS: electron microscopy, 2D crystallization, condensed matter, nanoparticles, ionic liquid

nall particles attached to a liquid interface are central to numerous technologies, from the stabilization of emulsions to the preparation of responsive coatings. 1-7 Much recent attention was directed at liquid interfaces decorated with nanoparticles (NPs) which, due to their small size, convey interfacial properties distinct from those delivered by larger particles. Beyond the electronic and optical characteristics inherent to nanoscale objects,8 functional NPs at liquid interfaces can experience readily triggered binding/ unbinding, robust in-plane mobility, and particle-particle interactions that are significant at distances comparable to, or even exceeding, the particle diameter. These characteristics underscore interfacial phenomena as varied as optical mirroring, selective chemical separation, and ferromagnetism. Some behaviors were recently realized through interfacial assembly and subsequent jamming of NPs strongly bound on dispersed drops; 10-12 because the number of bound NPs can increase during interfacial expansion but remains fixed during subsequent compression, cycles of expansion and compression trapped the drops into nonequilibrium, nonspherical shapes stabilized by their excess surface area. 13,14

Here, the structure and dynamics of densely packed, nearly monodisperse spherical NPs attached to a liquid surface were revealed at the single particle scale. A liquid cell was fabricated to control NP areal density, and in situ, scanning electron microscopy (SEM) imaging was conducted in real-time as PEGylated silica NPs of ~166 nm diameter were progressively unjammed and rejammed on ethylmethylimidazolium ethylsulfate [EMIM][EtSO₄], a relatively hydrophilic ionic liquid (IL). The IL's negligible volatility enabled long-term imaging even in the high vacuum of SEM. Experimental results are compared to existing simulation/theory predictions for dense packing, crystallization, and jamming of 2D spheres/disks. 15-19

Although many behaviors of NP-laden liquid interfaces are known, particularly in the context of Pickering emulsions, few reports describe how NPs pack or how they move across a liquid interface when their packing density is high. Many scenarios can be envisaged, but this study examines the packing order achieved upon stepwise compression of spontaneously jammed Gibbs monolayers of nearly hard sphere NPs. The monolayers are polycrystalline, and key questions concern the level of organization achievable, the mechanisms by which rearrangements improve organization, and the timeframes

Received: November 6, 2021 Accepted: March 21, 2022 Published: March 24, 2022





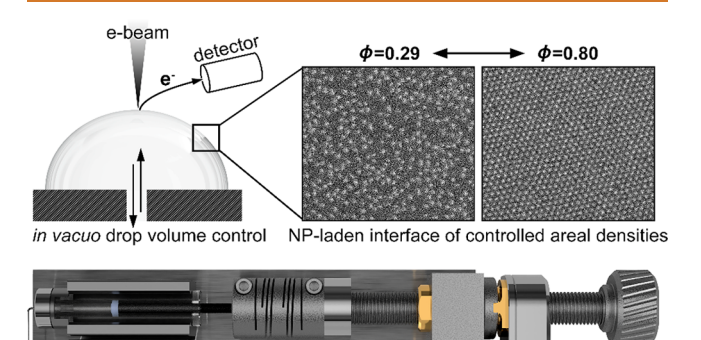
required for these rearrangements. For example, can a spontaneously jammed, modestly ordered NP monolayer be laterally compressed into a perfect (or near perfect) 2D crystal? This study also considered the practical limits to compression-induced monolayer rearrangements. When does monolayer compression produce out-of-plane deformations? Can sustained compression lead to irreversible changes to monolayer packing?

There are many literature reports of the properties of particle monolayers on liquid surfaces. 3-6,20-23 The compression/expansion of sphere monolayers, for example, has provided a simple physical model for the 2D ordering/ disordering observed in contexts from crystallization to jamming and vitrification. 23,24 Several techniques can probe static NP monolayer microstructure, with Langmuir-Blodgett methods perhaps the most popular. Typically, transferred monolayers are imaged ex situ as a function of the surface pressure that was applied as the layers formed. 20,25 On fewer occasions, X-ray reflectivity and small-angle X-ray scattering (SAXS) were conducted in situ to reveal packing features. 26-2 Monolayer dynamics were characterized by X-ray photon correlation spectroscopy (XPCS), for example, with an intermittent dynamical regime signaling a transition from diffusive to nondiffusive or confinement-dominated dynamics.²² Images of NP monolayers obtained by in situ atomic force microscopy (AFM) were compared to scattering intensities measured by grazing-incidence small-angle X-ray scattering (GISAXS) to confirm the structures visualized.³⁰

Many direct characterization techniques can perturb the "soft" NP microstructure at a liquid's surface, and less perturbative reciprocal space techniques offer only structural and dynamic information averaged over a large interfacial area. Therefore, to characterize the interfacial NP structures less ambiguously, a nonperturbative microscopy method that tracks individual NPs over large areas promises practical advantages and deeper insights. We recently developed an in situ, real-time scanning electron microscopy (SEM) method that exploits ILs as the NP liquid subphase.31 Our SEM approach roughly mimics the optical video microscopy methods established for the study of larger (i.e., size above the optical diffraction limit) dispersed particles.³² As a class of solvents, ILs resemble ordinary aqueous or organic liquids, dissolving and dispersing molecular and particulate species in predictable ways.³³ A few IL properties are noteworthy, particularly negligible volatility and finite electron conductivity, 34,35 both of benefit to electron microscopy imaging. An alternative electron microscopy approach, liquid cell transmission electron microscopy (TEM), sandwiches liquid specimens between solid windows. 36,37 While liquid cell TEM can probe NPs in liquids and at liquid-liquid interfaces, constraints on sample thickness, as well as interactions of liquid and/or NPs with the cell windows, can make such imaging cumbersome or impractical. Further, with one area imaged repetitively, NP dynamical studies are better suited to SEM, which employs less specimendamaging electron doses and lower electron energies.³⁸ By SEM, the 2D organization of NPs on a free liquid surface and the dynamics of each NP in an interfacial assembly can be tracked to the single particle level over surface areas encompassing tens of thousands of densely packed NPs.

Silica NPs were chosen for this project due to their relatively narrow size distribution and reasonable SEM contrast. Densely grafting relatively short (5000 g/mol) linear PEG ligands kept these NPs well-dispersed both in the bulk IL and at the IL—

vacuum interface.³⁹ The decreased surface energy of PEG relative to IL drove strong interfacial binding, with the binding energy of a single NP reaching thousands of $k_B T$.⁴⁰ By diffusion from bulk to surface, a jammed Gibbs monolayer formed on a fresh IL interface on a time scale of hours. NPs rarely, if ever, were observed to detach subsequently. Due to their polar PEG ligands, the bound NPs displayed a relatively small IL contact angle, pushing the greater part of each NP to reside below the IL surface, beneath the depth of SEM imaging. 39,40 Consequently, a ring of solvent outlined each NP in images of jammed/crystallized NPs. The aforementioned features made this IL-NP system ideal for exploring NP monolayers by SEM. The interfacial area of a supported IL drop was expanded/contracted using a customized liquid cell placed inside the SEM chamber. Figure 1 illustrates how the addition or withdrawal of liquid from the drop provided control of the IL interfacial area, which in turn, provided the change of NP areal packing density ϕ .



specimen stage with an orifice connected to a motorized syringe

Figure 1. Liquid cell for *in situ* SEM observation of interfacially compressed NP monolayers.

RESULTS AND DISCUSSION

Characterization and Interfacial Assembly of NPs. When packed at high ϕ , the PEGylated NPs displayed significant long-range translational and orientational order, due, in part, to their narrow size distribution, 5.3%, defined as the ratio of the standard deviation of the diameter to its mean. With conformation of the flexible PEG ligands experimentally ill-characterized and possibly altered at high areal compression, ϕ was calculated without considering their presence. Nonetheless, these ligands were responsible for the large interfacial NP binding energy as well as the repulsive NP interaction potential U(r) stabilizing the NPs sterically. The dilute solution radius of gyration of 5000 g/mol PEG in water is ~2.5 nm, 41 and, in various imidazolium-based ILs, PEG is reported to assume a Flory exponent similar to that in water, 0.55-0.60, 40 a value consistent with its good solvent character. By the "grafting-to" approach adopted to attach the PEG ligands, only a modest NP grafting density was achieved, ~0.5 chain/nm², which corresponded to an average distance D between anchoring sites of ~1.6 nm. According to the classic Alexander-de Gennes theory, 28 end-grafted polymers form a stretched brush when their segmental density exceeds that of a semidilute solution, reached for 5000 g/mol PEG in water when the polymer volume fraction goes above ~0.08. 42 By the same theory, a brush's volume fraction is given by $(a/D)^{4/3}$,

where a is the effective segment size. For PEG, previous experiments showed that a is \sim 0.28 nm, 41 and for the chosen molecular weight, the number N of segments in a chain is \sim 90. For these parameter values, the NP ligands are inferred to form a short brush, and by the same theory, the uncompressed thickness $L_{\rm o}$ of this brush is given $aN(a/D)^{2/3}$, \sim 8.1 nm. The contribution of ligands to NP diameter is, therefore, comparable to the uncertainty in diameter associated with NP polydispersity.

The PEG ligands also provide the NPs with a low contact angle, ~14°. The gravitational force on particles smaller than the capillary length is insufficient to deform the IL interface significantly, and so, to adopt this contact angle without a meniscus deformation, the NPs were preferentially displaced toward the IL, leaving only a protruding spherical cap surrounded by an essentially planar liquid surface.⁴⁰ Consequently, the NPs interacted with each other principally along their submerged equators, where the ligands necessarily retained their bulk conformation due to the large distance to the surface. The ligands grafted near the contact line, and thus closer to the surface, were probably stretched outward across the interface because of PEG's low surface energy; the surface energy of PEG against vacuum, 43 mJ/m², is significantly less than that of IL against vacuum, 48 mJ/m². Reflecting the contributions from their many surface-attached ligands, NPs bound to the surface with an energy of \sim 1400 $k_{\rm B}T$ per NP as measured by pendant drop tensiometry. Owing to the large magniture of this energy, NPs from a bulk dispersion rapidly saturated a fresh IL interface, forming a dense Gibbs monolayer, and unless highly compressed (to ϕ greater than 0.85), no NPs were observed to detach from the surface.

When NPs saturated the interface, their areal density ϕ , calculated $\pi a^2 N_s / S$, where N_s / S is the NP areal number density, was ~0.77, well above the onset of local interface ordering, which occurred when ϕ was ~0.69. Both densities were significantly less than ϕ for a perfect 2D packing of monodisperse spheres, ~0.91.¹⁹ While clearly affected by packing imperfections, ϕ was also systematically reduced by the failure to account for the interfacial area occupied by ligands, and to a lesser extent, by the lack of account for small polydispersities in NP size and shape. At $\phi \sim 0.77$, the lattice constant determined from the radial distribution function g(r)was 2.06a, and if this distance is taken as the effective NP diameter, the areal fraction ϕ_{eff} at saturation was ~0.83, close to the simulated threshold for collective jamming of monodisperse 2D disks, ~ 0.86 . After the interface became saturated, ϕ did not change for several hours, the longest experimentally accessible time period, and lateral motion was undetected, revealing that the NPs were jammed.

As reported previously, 40 U(r) for the PEGylated NPs displayed a weak attraction, manifested in an energy well of depth $\sim 0.1~k_{\rm B}T$ at r of order a, and this attraction was tentatively ascribed to capillary interactions arising from ligand-induced menisci. These menisci have not yet been confirmed. Nonetheless, the attraction was too weak to have meaningful consequence here, and therefore NP packing was dominated by hard-sphere interactions, as slightly modified at small NP separation by the PEG brush layer. At a fresh IL interface, NPs spontaneously packed as a dense Gibbs monolayer lacking large voids or wrinkles, and before eventual jamming, the NPs displayed obvious Brownian motion. For monolayers not strongly compressed over an extended time, subsequent areal expansion would drop ϕ below the threshold

for local ordering, and the lattice would then melt, leaving single NPs stably dispersed across the interface. This melting transition, observed at $\phi \sim 0.68$, was manifest in translational and orientational order parameters as well as g(r), as discussed in the Supporting Information.

A typical SEM image of a saturated NP monolayer at $\phi \sim$ 0.80 is shown in Figure 1. Well before saturation, the NPs had rapidly assembled from the subphase, due to a favorable interfacial binding energy, but approaching saturation, the unfavorable interactions of a bound NP with its neighbors created an energy barrier, which hindered binding of additional NPs. Eventually suppressing further adsorption of the NPs to the surface, coinciding with the point of interface saturation. As demonstrated in the Supporting Information, the average separation between adjacent NPs in a saturated monolayer was ~6 nm, sufficient to create NPs a repulsive pairwise interaction of \sim 200 $k_{\rm B}T$ for neighboring NPs. With a nominal six nearest neighbors, the in-plane energy cost reached \sim 1200 $k_{\rm B}T$, approximately equal to the attractive 1400 k_BT attained by binding to the bare liquid surface. Responding to the in-plane repulsions, an NP might shift slightly above or below the plane of the interface without detaching, explaining why detachments were not observed until a saturated monolayer was further significantly compressed. Since SEM at low voltage (3 kV) could discern only surface features or subphase structures within ~5 nm of the IL surface, 31 each NP appears as a bright circle against a dark IL background. The low contact angle makes the circles smaller than the actual NPs. The depth resolution was insufficient to ascertain whether any NPs resided slightly above or below nearby NPs.

NP Structural Rearrangements after Monolayer Compression. Liquid withdrawals/additions from/to a small IL drop supported on a smooth polytetrafluoroethylene-covered flat substrate varied the drop's interfacial area. After a jammed Gibbs monolayer was established on a fresh drop, withdrawals led to drop shapes different from that predicted by the Young-Laplace equation, specifically, shapes flatter near the drop crest. The IL-vacuum-substrate contact line receded smoothly during withdrawals, with the receding contact angle lower than the starting quiescent contact angle. SEM visualizations showed that ϕ across the compressed interface was not uniform, especially right after a stepwise compression. All these observations are attributed to the high resistance to area reduction by the jammed NP monolayer. Modeling compression of a nonlinearly elastic interface supported on a spherical liquid cap of diminished volume, the area reduction and interfacial stress near the crest were predicted to be almost spatially uniform, 43 consistent with the SEM observation of uniform ϕ in this region. Since the surface near the crest was flattened, imaging at that position was simplified. The motor responsible for the fluid exchanges was turned off during imaging to eliminate motions of the liquid cell. After a stepwise compression, monolayer structural rearrangements at the drop crest continued for tens of minutes due to the slow relaxation of interfacial stress. 44,45 For small compressions, this area's jammed interface remained almost flat, lacking out-of-plane distortions.

Packing rearrangements of a jammed NP monolayer after a small stepwise area compression (<2% area change) are shown in Movie S1. For this monolayer, ϕ was well above the threshold for local crystalline order, with various packing defects as well as regions of disorder apparent across an interfacial area encompassing more than 10,000 NPs. Despite

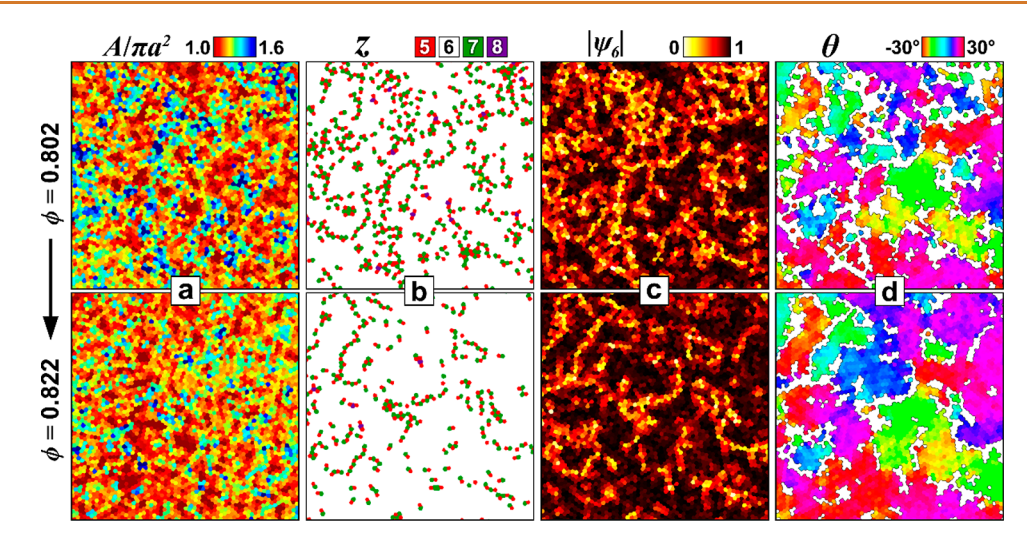


Figure 2. Maps of local order metrics for an NP monolayer before and after interfacial compression. (a) Voronoi cell area normalized by NP cross-sectional area, $A/\pi a^2$. (b) Coordination number z. (c) Bond-orientational order $|\psi_6|$. (d) Local hexagonal orientation θ . Top row: $\phi = 0.802$, t = 0 s and bottom row: $\phi = 0.822$, t = 180 s. Image widths are 5 μ m.

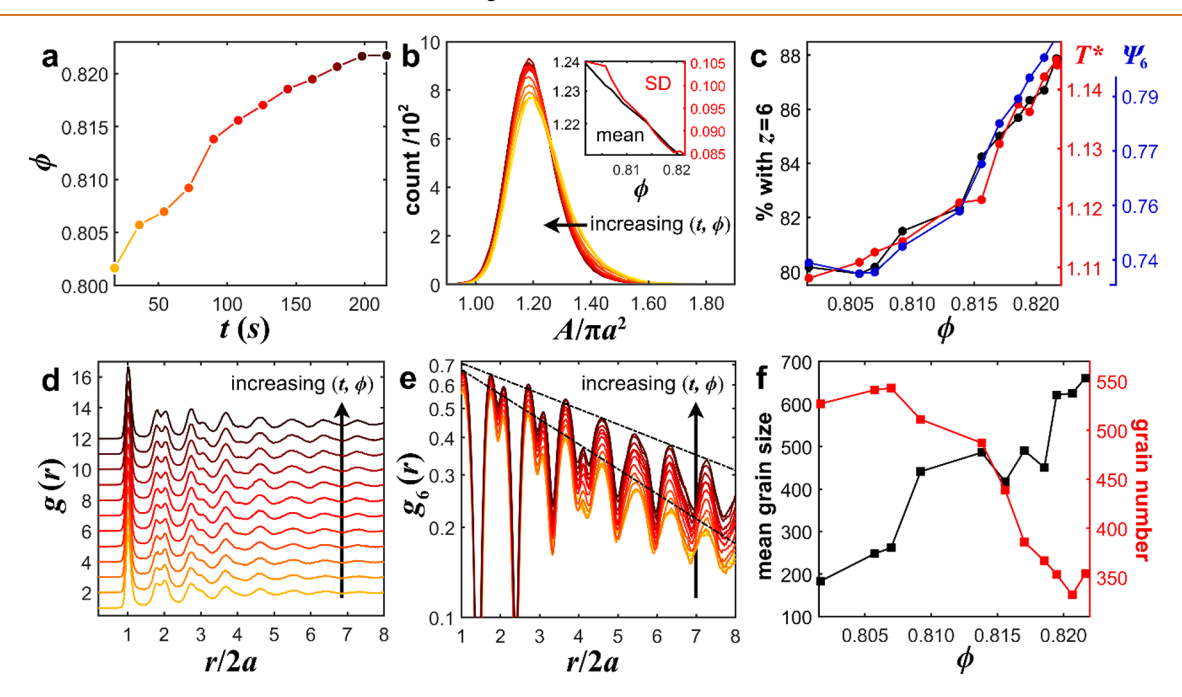


Figure 3. Structural ordering after compression: (a) ϕ plotted against t; (b) histogram, as well as mean and standard deviation, of normalized Voronoi cell area for increasing t and ϕ ; (c) order metrics T^* , Ψ_6 , and percent with z=6 plotted against ϕ ; (d) g(r) as a function of t and ϕ ; (e) $g_6(r)$, the spatial correlation function of $|\psi_6|$, as a function of t and ϕ . Dashed lines are fits to $-\exp(-\lambda r/2a)$ for t=0 and 234 s. (f) Mean grain size and grain number plotted against ϕ . Colors of (t, ϕ) pairs are matched across panels a, b, d, and e.

significant NP motion, the structure was grossly retained as the monolayer relaxed from the compression. All imaged NPs displaced by distances of a or greater during and after the compression, but they rarely attached or detached from the interface. The load-bearing NPs in the monolayer broke jamming by a collective swirling-type motion, and, afterward, NP configurations evolved by similar motions to reduce the excess in-plane internal stress. This evolution proceeded across the time window imaged. Several fixed time point analyses of starting, t=0, and near ending, t=218 s, configurations are summarized in the images of Figure 2a–d and Movie S2, which offer maps of several key packing metrics; the top configuration maps in the figure are for t=0 with $\phi=0.802$, and the bottom ones are for t=218 s with $\phi=0.822$.

Figure 2a maps the normalized Voronoi cell area $(A/\pi a^2)$; Figure 2b maps the NP coordination number z; and Figure 2 panels c and d map the local bond-orientational order parameter $|\psi_6|$, and the local hexagonal orientation θ , respectively. The mapped metrics, standard to 2D sphere packings, will be defined later.

The before and after maps of Figure 2a–d demonstrate complex, compression-initiated shifts in NP structure, leading to denser packings, reduced defects, enhanced hexagonal order, and larger grains. On the grain size scales, both density and order fluctuated. Throughout the changes, SEM tracked each NP center position to a spatial resolution of \sim 3 nm. The densification shown in Figure 2a reflects an influx of NPs from the unimaged drop periphery, where ϕ after the surface

compression was greater than at the crest; initial recession of the contact angle overcompressed the NPs in peripheral regions, pushing NPs slowly toward the crest. However, this large-scale displacement was insignificant when assessed against the less regular local NP displacements associated with configurational rearrangements.

Figures 3a-f highlight the t-dependence of the structural rearrangements visualized in Movie S1. To indicate the progression in t, data in several of these figures are colored from yellow to black. Figure 3a tracks ϕ growth, which during the process of rejamming increasingly slowed as ϕ increased; the time for the restoration of constant ϕ cannot be pinpointed due to the limited observation window, but this time was in the range of several minutes. The concurrent growth in packing order is evidenced in Figure 3b, which presents the distribution of normalized Voronoi cell area, spanning ~1.10 to ~1.60; this lower limit of this parameter is reflected in the local packing of the NPs into a perfect lattice, where $A/\pi a^2 = 1/\phi = 1/0.91 =$ 1.10. Due to size polydispersity, hexagonal packings of NPs smaller than the average diameter resulted in $A/\pi a^2$ as low as ~1.0. As order improved under relaxing interfacial stress, the distribution of cell area shifted downward and narrowed, demonstrating that a denser packing is associated with increased local order. The mean and standard deviation of the distributions are given in the inset to Figure 3b; the areal average of $A/\pi a^2$, of course, is exactly equal to $1/\phi$ irrespective of NP organization; the standard deviation, reflecting the uniformity of local packing, dropped in close correspondence with normalized area, showing that fluctuations in local packing density occur at length scales limited by the average normalized Voronoi cell size.

The topological defects of a 2D crystal are disclinations (extra or missing 60° wedge) and dislocations (half-row of NPs removed from the lattice).⁴⁶ After Voronoi tessellation, NPs with $z \neq 6$ pinpoint the former, while bound pairs of z = 5 and z = 7 disclinations distinguish the latter. As illustrated in Figure 2b, isolated disclinations did not appear in the spontaneously assembled NP monolayers due to their large elastic energy, but dislocations significantly populated grain boundaries, helping to mediate the differing angles of neighboring lattices; a comparison of Figure 2b and Figure 2d clearly indicates that dislocations well delineated grain boundaries. The increased percentage of NPs with z = 6 indicated in Figure 3c demonstrates that topological defects were systematically annihilated over the same period after compression that characterized the densification evident in Figure 3a,b. Due to their large excess free area $(A/\pi a^2 \gtrsim 1.4 \text{ for each disclination})$, dislocations were highly susceptible to surface pressure. Figure 2b shows a relatively small number of NPs displaying z = 8, their occurrences diminishing rapidly after the compression (data not plotted due to insufficient statistics); these NPs were always associated with the strings of dislocations at grain boundaries.

The complex bond-orientational order parameter ψ_6 is calculated for NP k at position r_k from the set of angles θ_{kj} constructed between an arbitrary fixed axis and lines drawn through the NP and each of its n_b nearest neighbors, 17

$$\psi_6(r_k) = \frac{1}{n_b} \sum_{j \in \mathcal{N}_b} e^{6i\theta_{kj}}$$

The absolute magnitude of ψ_6 , written $|\psi_6|$ and ranging from 0 to 1, measures the degree of local hexagonal order for NP k,

and the average of ψ_6 over all NPs, Ψ_6 , measures the degree of local hexagonal order across the system. Topological defects systematically had $|\psi_6|\lesssim 0.75$, while NPs in crystalline domains (all with z=6) had $|\psi_6|\approx 0.90$. The large value of the latter indicates that most structural disordering at high ϕ arose from topological defects, a conclusion consistent with the strong correlation between Ψ_6 and the percentage of NPs with z=6 noted in Figure 3c. After compression, Ψ_6 increased from 0.73 to 0.81, near the ensemble average predicted for collectively jammed disks, 0.86, and, unsurprisingly, larger than that computed for the maximally random jammed (MRJ) configuration, 0.68.

The translational order metric T^* , derived from g(r), summarizes local correlations of radial position, ¹⁸

$$T*\frac{\int_{2a}^{r_c} |g(r) - 1| dr}{r_c - 2a}$$

where $r_{\rm c}$ is a cutoff distance, chosen as $3\rho^{-0.5}$, where ρ is the sphere areal number density. For this cutoff choice, T^* quantifies the degree to which a packing locally departs from random, that is, characterized by $g(r) \neq 1$ on a scale of $\sim 3-4$ NP diameters. Figure 3c plots the evolution of T^* alongside that for Ψ_6 . Although, Ψ_6 and T^* manifest distinct aspects of monolayer structure evaluated at different local length scales, the two metrics are strongly correlated. For a 2D sphere packing, neighboring hexagonal local cells interlock with each other so that they cannot rotate appreciably relative to each other to release short-range positional order. Orientational and positional order are thereby reinforced over the scale of few NP diameters.

As seen in Figure 3d, g(r) shows peaks at the relative rpositions expected for a triangular lattice of packed spheres.¹⁹ With increasing t and ϕ , peaks at larger r became more prominent, and the second peak, at $r/2a \sim \sqrt{3}$, grew in magnitude compared to surrounding peaks; this peak originated in hexagonally close-packed four-particle arrangements. These g(r) trends re-enforce the trends discussed in the context of Figure 3c. The first peak, at $r/2a \sim 1$, reflects NP-NP close contacts, and when these contacts were squeezed at higher ϕ due to brush layer compression, this peak shifted to slightly smaller r, from ~ 6.05 nm to ~ 4.57 nm. From the Alexander-de Gennes model of ligand-mediated repulsive interactions (see Figure S1 and surrounding discussion), the pairwise NP interaction energy established under this compression grew from $\sim 3 k_b T$ to $\sim 1100 k_b T$, the latter still smaller than the NP interfacial binding energy. While this calculation assumed spatially uniform lattice compression, the actual local stress field depended on the nonuniform local packing configuration. When a compression pushed ϕ beyond ~0.82, a few NPs were expelled into the liquid subphase, mostly from crystalline domains, where the interparticle stress field was expected to be greatest. Despite the high elastic energy stored at dislocations, due to the free surface area nearby, NPs were not expelled from the interface but instead rearranged to annihilate the defects.

Spatial persistence of hexagonal order is captured in the ψ_6 correlation function $g_6(r)$,

$$g_6(r) = Re\{\langle \psi_6^*(\mathbf{r}_k)\psi_6(\mathbf{r}_l)\rangle_{|\mathbf{r}_k-\mathbf{r}_l|=r}\}$$

where the average is taken over all NP pairs (k, l) satisfying the condition $|\mathbf{r}_k - \mathbf{r}_l| = r$. Ignoring lattice peaks, Figure 3e shows that $g_6(r)$ decays almost exponentially for $r/2a \gtrsim 3$. Grain

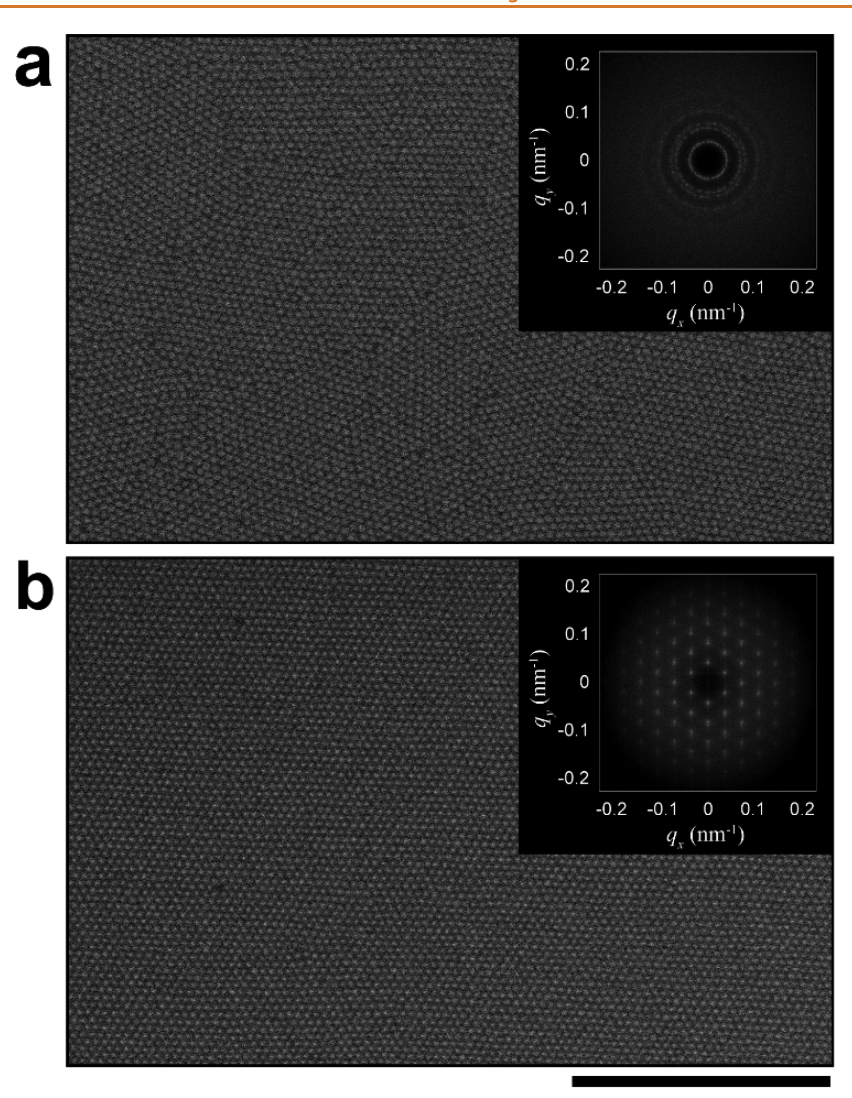


Figure 4. Images of an NP monolayer before and after interface compression (a) as spontaneously saturated by NP adsorption, at $\phi \sim 0.80$, and (b) after compression and equilibration to $\phi \sim 0.90$. Insets shows 2D fast Fourier transforms. Scale bar is 5 μ m.

growth after compression expanded the persistence of hexagonal ordering, and the spatial decay length λ , determined by fitting $g_6(r)$ peaks to $\exp(-r/\lambda)$, decreased from 10.5a to 16.7a during the 218 s of Movie S1. Consistent with these trends, the same figure shows that hexagonal order at longrange was more enhanced by compression than at short-range, where hexagonal order was high before the compression. Grains, varying in size and orientation, as expected for a 2D polycrystal, are apparent in the maps of Figure 2b-d. In Figure 2d, which most clearly distinguishes grains, Voronoi cells with $|\psi_6| > 0.75$ are colored by their orientation, calculated as $\theta \equiv$ $1/6 \arg(\psi_6)$, which is defined over the range $-30^\circ \le \theta \le 30^\circ$. Sharp shifts in orientation are observed across grain boundaries while more gradual shifts are noted across the interiors of a few grains. To highlight grains better, Figure S3 uniquely colors each group of more than three adjacent NPs for which $|\psi_6|$ > 0.75 and θ varied by <2°. Misorientations greater than the 2° threshold were highly concentrated at the dislocations on grain boundaries, with just a few misorientations inside the uniformly colored domains; the dislocations, presented in black, are seen to outline the grains.

The average standard deviation of θ for the crystalline grains defined in Figure S3 was 1.3°, and this parameter had no clear

dependence on t or ϕ . Thus, orientational order inside the grains was little affected (*i.e.*, improved) by interfacial compression. Nevertheless, as shown in Figure 3f, the weight-average grain size, defined $\sum M_i^2 N_i/M_i N_i$, where N_i is the number of grains containing M_i NPs, increased over the course of Movie S1 from 180 to 660. Under a compression raising ϕ to ~0.90, a single domain containing more than ~10⁵ NPs could be obtained over an interfacial area greater than the 50 μ m × 50 μ m region imaged by SEM. Part of one such domain is shown in Figure 4b, and the associated Fourier transform is provided in the figure's inset. For comparison, Figure 4a presents the jammed monolayer in its precompressed state at $\phi \approx 0.80$; numerous defects and little indication of long-range order are evident.

NP Motions during Structural Ordering. Turning again to analysis of Movie S1, Movie S3 plots as arrows the NP displacements $\Delta \mathbf{r}$ accumulated over successive single time steps of duration Δt , the 18 s interval between frames. Figure Sa likewise presents $\Delta \mathbf{r}$ for one typical time step, that at t=54 s. Consistent with the ϕ growth outlined earlier, arrows near the periphery are noticed to point inward with slight preference, but everywhere, locally correlated fluctuations of arrow direction and length dominate. The associated collective

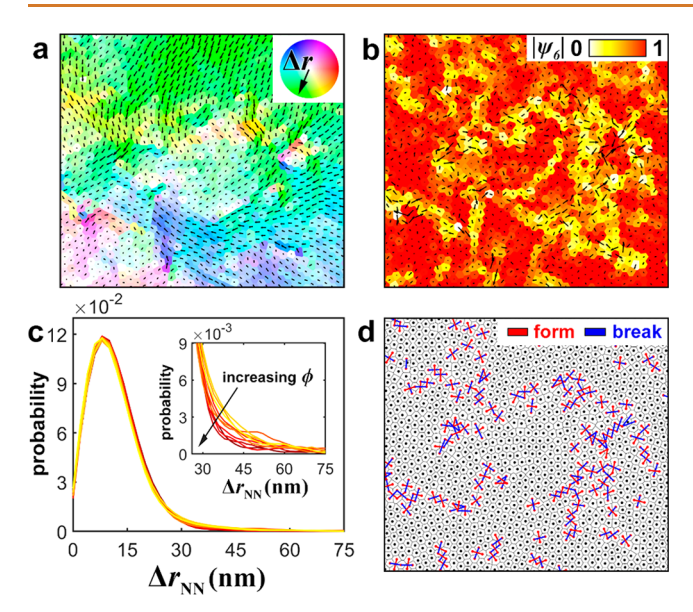


Figure 5. NP motions after compression. (a) Map of one-step displacements for t=18 s. Cell color indicates direction (hue) and distance (brightness; maximum displacement is 150 nm). (b) Map of the relative displacement $\Delta r_{\rm NN}$ of each NP center with respect to nearest neighbor NPs. Arrows are twice the length of actual displacements. Voronoi cells are colored by $|\psi_6|$. (c) Distribution of $\Delta r_{\rm NN}$ plotted for different ϕ . Inset: distribution enlarged for $\Delta r_{\rm NN} > 30$ nm. Curves are colored according to (t, ϕ) pairs as in Figure 3. (d) Mapping of the formation and breakage of NP bonds determined by Delaunay triangulation.

NP swirling was both intermittent and spatially heterogeneous. The length scales of the correlated fluctuations were comparable to the sizes of the ordered domains. Previous experiments and simulations of jammed systems under load exhibited similar dynamics, often finding motions driven by slow build-up and rapid release of stress. 48,49 This dynamical intermittency characterizes dense systems alternating between

jammed and unjammed states under a load slightly above the yield stress. After a slightly larger compression than used in making Movie S1, the cooperatively rearranging regions (CRRs) noted here transformed from large patches (at $\phi \sim 0.80$) to strings (at $\phi \sim 0.82$). Consequently, under larger load the CRR sizes decreased even as their lifetimes increased.

Motions of an NP and its nearest neighbors can be highly correlated. To assess the correlation for the displacements mapped in Figure 5a, the relative displacement $\Delta r_{k,\rm NN}$ of NP k was obtained by subtracting the average displacement of z nearest neighbors from the NP's own displacement,

$$\Delta \mathbf{r}_{k,\text{NN}}(t) = \Delta \mathbf{r}_k - \frac{1}{n_b} \sum_{j \in N_k} \Delta \mathbf{r}_j(t)$$

Figure 5b overlays the maps of Δr_{NN} and $|\psi_6|$. Unsurprisingly, the two maps display a strong correspondence; transport (i.e., relative displacement) along grain boundaries is much more rapid than that through lattices. 50 For NPs associated with a dislocation, $\Delta \mathbf{r}_{NN}$ was typically $\gtrsim 30$ nm, while inside lattices, Δr_{NN} was typically $\lesssim 10$ nm. Figure 5c presents evolution of the $\Delta \mathbf{r}_{\mathrm{NN}}$ histograms with growing ϕ , and the inset magnifies trends in these histograms at larger $\Delta r_{\rm NN}$. As ϕ increased, $\Delta r_{
m NN}$ in lattices, where this parameter is smallest, changed little (main plot), but $\Delta \mathbf{r}_{NN}$ in less ordered surroundings, where this parameter is larger, dropped noticeably (inset plot). For the latter regions, large $\Delta \mathbf{r}_{\mathrm{NN}}$ was often achieved by the breaking of bonds defined by Delaunay triangulation. Figure 5d maps the breaking/forming of bonds, and comparing this map to the one for Δr_{NN} the same crystalline grains are identified. The key finding from Figure 5 re-enforces the key finding from Figure 3; after a stepwise compression, NP monolayers slowly relieved excess mechanical stress through intermittent correlated motions that increased the average size of ordered domains.

Over t larger than that between successive frames, NPs rearranged their packing over greater (*i.e.*, >a) but still not long-ranged length scales. For example, the maps of Figure 6a, corresponding to displacements accrued over 126 s, show

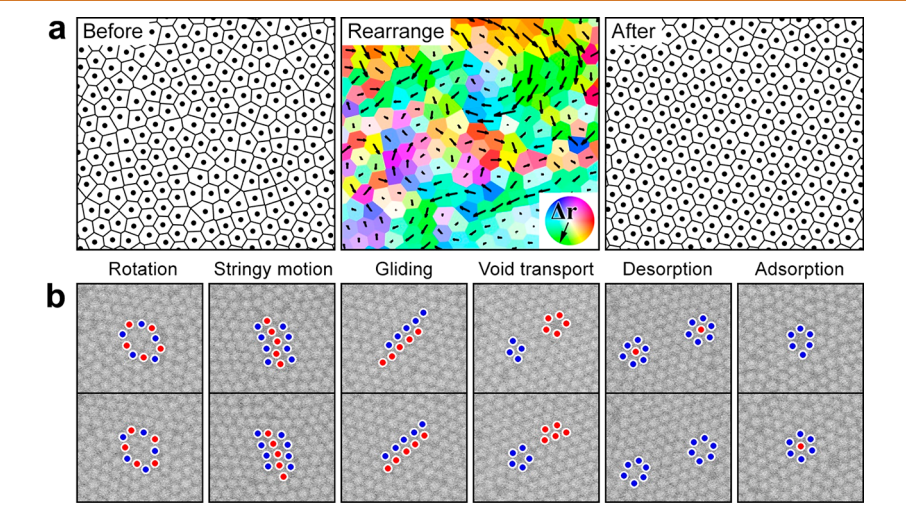


Figure 6. Local NP rearrangements after interface compression. (a) NP displacements (center mapping; Voronoi cells colored by Δr) that reveal the cooperative motions of NP domains to achieve lattice ordering. These displacements are compared to NP configurations before (left mapping) and after (right mapping; t = 126 s) the compression. Box widths are $3.1 \,\mu m$. (b) Tracked NP lattice positionings that display local rotation (a cluster surrounded by red and blue circles is rotating in a clockwise direction), migration of string-like clusters (a string of red circles are moving downward in respect to surrounding blue circles), lattice gliding (lattice glides in a diagonal direction along the boundary between red and blue circles), vacancy displacement (vacancy in red circles is displaced into blue circles), and NP desorption/ adsorption (red circles disappear/appear). Box widths are $1.8 \,\mu m$.

several irregularly defined NP clusters, up to ~8 NP in diameter, that rotated within a relatively disordered region (see the first map) to form a single, well-ordered domain of ~400 NPs (see the third map). The displacement field for the rearrangement (the second map) highlights ~5 distinct swirls that rotated the clusters into registry. As the single large domain emerged, NP displacements were relatively small at vortex centers and between adjacent clusters that rotated in a common direction (i.e., either both clockwise or both counterclockwise); over the same period, NP displacements were greatest between adjacent clusters that rotated in opposite directions. Different classes of local lattice rearrangements were also observed, as summarized in Figure 6b, including (i) rotation of a closed NP cluster around a nearly undisplaced NP core, (ii) slippage of a line of NPs along a lattice direction, (iii) gliding between adjacent lines of lattice NPs, and (iv) filling of a vacancy by neighboring NPs to create a new vacancy displaced from the original in the direction of the local compression gradient. Lastly, NP desorption/ adsorption could affect local hexagonal order, as also indicated in Figure 6b. Adsorption was rarely observed since most voids were too small at such high ϕ to accommodate an additional NP. Desorption of a lattice NP was only observed after a larger interfacial compression than the one that produced the relative displacement maps of Figure 5.

Film Mechanical Instability and Ligand Entanglement. Larger withdrawals from the underlying fluid drop than considered in earlier discussion led to jammed monolayers of the appearance depicted in the uppermost left images of Figure 7. Large withdrawals induce hoop stresses on a drop surface sufficient to create radial monolayer wrinkles. The wrinkling was observed over a range of wavelength λ ; Fourier transforming the wrinkles of Figure 7 away from the drop's center of symmetry, in a region where the wrinkles are nearly parallel, revealed that 3 $\mu m \lesssim \lambda \lesssim 86 \mu m$. Modeling the monolayer as an isotropic elastic film of thickness h equal to 2a, classical elasticity theory predicts that λ follows⁵

$$E = \frac{3}{4\pi^4} \frac{\rho g (1 - \nu^2) \lambda^4}{h^3}$$

where E, ν , and h are the film's elastic modulus, Poisson ratio, and thickness, respectively, and ρ is the subphase fluid density. S1,S2 The distortion of packing for 2D spheres in a rhombic unit cell leads to $\nu \approx 1/\sqrt{3}$. Combining these equations, approximations, and parameter values, the theory predicts that 750 kPa $\lesssim E \lesssim 0.7$ kPa for the wrinkled NP monolayers of Figure 7.

For a liquid-supported interfacial layer combining liquid and dispersed rigid particles, E can be expressed solely as a function of the liquid's surface tension γ and h,

$$E = \frac{1 - \nu}{1 - \phi} \frac{\gamma}{h}$$

if ϕ remains constant during a small interface deformation, as naively expected for strongly bound NPs. 51 Inserting known or predicted values of ν , γ , and h, this expression provides $E \approx$ 815 kPa, consistent with $\lambda \sim 87~\mu\text{m}$, close to the largest λ calculated. There is evidence, 53 however, that ϕ may not be constant under compression, with NP in a jammed monolayer pushed up and down from the interfacial plane; the NP contact angles under mechanical stress may thereby not match their values at adsorption equilibrium, 53 leading to complex, t-

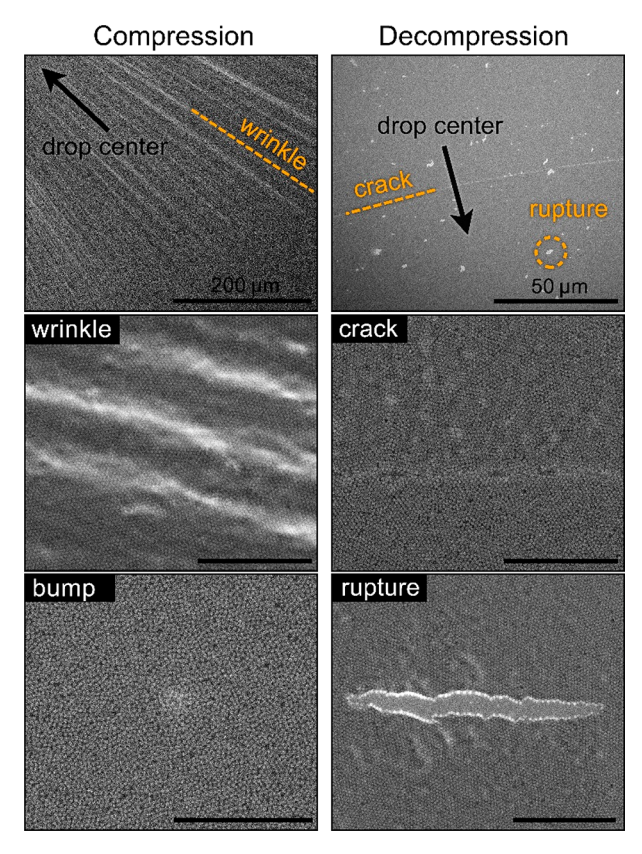


Figure 7. NP monolayer instabilities manifested after a large amplitude 6-h compression and then after a subsequent reexpansion. (Left row) Low-magnification images, taken after the compression, showing wrinkles and bumps. (Right row) Lowmagnification images, taken after the subsequent re-expansion, displaying cracks and local ruptures. Bottom two images are enlargements from areas indicated in the top image. Scale bars are $5 \mu m$ except as noted.

dependent mechanical behaviors.⁵⁴ For the low initial contact angle here, $\sim 14^{\circ}$, E at small t could have been significantly softened by downward NP displacements,⁵⁴ explaining the broad distribution of λ . The wrinkles did not extend to the drop center, but their outward ends formed a circle defined by a lower bound to the compressive hoop stress needed for wrinkling. At the drop center, the compressive stress was relieved by several small bumps of the type seen in the lowermost left image of Figure 7. To form such bumps, the hexagonal lattice must locally distort into an outward-oriented tetragonal lattice.

Increasing drop volume to reverse interface compression, wrinkles and other out-of-plane instabilities usually disappeared rapidly, with the original smooth drop shape fully recovered if the period of compression had not been long. The melting of compression-induced polycrystals was much slower, with large, striated cavities formed initially, as illustrated in Figure S4. The expanded 2D monolayer then slowly rearranged to fill, or heal, the cavities, thereby rebalancing disparities in surface pressure. These rearrangements are captured in Movie S4. Different behaviors were observed when the monolayers were kept at high compression for several hours or more; then, when the aged monolayer was expanded, long cracks and ruptures opened instead of cavities, as demonstrated in the rightmost images of Figure 7. The top image reveals cracks perpendicular to the wrinkles just

described. Cracks and ruptures produced at these conditions were further distinguished by their failure to fill subsequently. This different behavior is attributed to the slow development of strong interparticle cohesion under sustained high compression. The origins of the cohesion are unclear. One possibility is entanglement of PEG ligands from different NPs; simulations and experiments suggested that low graft densities can foster ligand interpenetration and increase monolayer toughness.55

Potential Control of 2D Structural Rearrangements in Jammed NP Monolayers. Tailoring the structure and properties of NP interfacial monolayers has obvious ramifications for technologies that rely on the monolayers to stabilize liquid interfaces. However, the assembly of such monolayers, as well as their response to interfacial mechanical forces (such as compression), has not before been visualized. Low and modest compression, rather counterintuitively, facilitated localized NP rearrangements necessary in a jammed monolayer to enhance crystalline grain size. The ability to generate near perfect crystals in this fashion was surprising. Key to these rearrangements were the NP ligands, which endowed the NPs with limited softness, expressed at length scales much smaller than the NP size. The flexible ligands essentially absorbed a modest compression while the overall monolayer integrity was maintained. True hard spheres, not yet experimentally available in this interfacial context, would likely have behaved differently, as would spheres with greater softness, that is, longer ligands. Studies that vary ligand length relative to NP diameter could explore this problem to greater depth than was possible here. A particular size ratio may be optimal for most easily achieving single crystals of large span.

That saturation and jamming achieved simultaneously is a second surprising finding. By creating patches of "free area" of appropriate size, localized NP motions in disordered regions furthered NP binding in already dense monolayers. One could equally envisage that dense but unjammed packings could admit only NP motions that disallow such binding, making ϕ at saturation lower than ϕ at jamming. More precise studies might show differences in the two critical ϕ values or whether the commonality observed here extends for other ratios of NP to ligand size or to NPs with lower binding energies and/or different shape. The propensity of spherical NPs to crystallize at ϕ well below saturation and jamming likely plays a central role in the behavior observed. Differences in the two critical values would define a range of ϕ over which disordered monolayers would be saturated but not jammed, that is, liquidlike. Going a step further, regulating NP attachment/ detachment could be exploited as means to control the rate of 2D structural rearrangements in NP monolayers that would otherwise be jammed.

CONCLUSIONS

Rearrangements of NPs in dense Gibbs monolayers compressed or expanded at a liquid surface were investigated to the single particle level by in situ SEM. Strong NP interfacial attachment, high in-plane NP mobility, and nearly hard-core NP-NP interactions led spontaneously to polycrystalline 2D packings that jammed before the interfacial mechanical stress was applied in stepwise fashion. NP rearrangements were monitored over interfacial areas containing tens of thousands of NPs. The time evolution of packing was captured in maps of metrics such as $A/\pi a^2$, z, Ψ_6 , and T^* as well as dislocation positions. After low and modest compressions, monolayer

ordering was associated with shearing along the dislocations concentrated at grain boundaries. At the same compressions, but at larger length scales, motions of ordered clusters, that is, small grains, were both strongly correlated and highly transient, and these entities grew by rotational alignment and subsequent attachment to neighboring clusters. The intermittency and heterogeneity of the motions suggest fluctuations between yielding and jamming under imposed stress. Subject to appropriate compression and left long enough, a relatively disordered initial microstructure transformed into a single crystalline domain with very few defects. At larger compression (those leading to $\phi \gtrsim 0.9$), out-of-plane deformations such as wrinkles and bumps appeared. After short periods of small or modest compression, re-expanded monolayers opened small cavities, which rapidly healed. However, after many hours under the same or large compression, an NP monolayer solidified, and when its interfacial area was then re-expanded, irreversible long cracks or open ruptures emerged. These experimental observations provide insights into the mechanism of interfacial NP assembly, the response of interfacial NP assemblies to nondilatational and dilatational stresses, and the mechanisms by which translational and orientational defects in NP monolayers can be erased under compression to create nearly perfect 2D crystals.

MATERIALS AND METHODS

In Situ SEM Liquid Cell. The SEM liquid cell, pictured in Figure S5, allowed nanoscale visualization as well as mechanical manipulation of soft microstructures at an open liquid interface. A drop of nonvolatile liquid was placed on the cell's flat specimen stage, which had a hole at its center, and liquid additions/withdrawals through this hole varied the drop volume and thereby the drop interfacial area. Additions/withdrawals were controlled by a linear screw-type actuator (Physik Instrumente, N-470.U) connected to a glass syringe; the pair acted together as a syringe pump. A piece of PTFE tape (3M 5480 PTFE), attached by a silicone adhesive to the mirror-finished aluminum specimen stage, was replaced before each experiment; the tape was punctured above the hole in the stage to allow liquid in/out of the drop. The tape made the overlying drop adopt a high contact angle. The syringe needle (Hamilton 1725 series 22s gauge, 250 μ L, cut in 25 mm length) was epoxy-glued (J-B Weld Twin Tube) to a sidewall port drilled to the stage's center hole. The entire 30 mm wide × 95 mm long × 22 mm high liquid cell easily fit within the SEM chamber.

Specimen Preparation. Silica NPs coated with 5000 g/mol PEG were prepared as described in a previous work.³¹ TEM examination of 900 dried NPs found that their average diameter was 166 ± 9 nm. The NPs were centrifuged and redispersed in methanol multiple times to remove soluble contaminants, particularly unattached PEG. The final methanol dispersion contained NPs at a concentration of ~20 mg/mL. To prepare a SEM liquid cell specimen, an \sim 8 μ L IL drop was placed on the punctured PTFE film. The IL, 1-ethyl-3methylimidazolium ethylsulfate ([EMIM][EtSO₄], 99% purity), was purchased from Iolitech and used without purification. Onto the drop surface, 2 μ L of the washed methanolic NP dispersion was carefully spread, and immediately afterward, the two liquids partially mixed near the surface before the methanol fully evaporated. The SEM liquid cell was kept in a vacuum oven for several hours afterward to remove residual methanol and traces of water from the drop (the IL is

Volatiles or bubbles in the SEM liquid cell could burst, propelling IL into the SEM chamber. To prevent these occurrences, the IL had to be degassed completely. The specimen stage and syringe were first filled with IL and placed overnight in an ultrahigh vacuum chamber. After attaching these components to the rest of the liquid cell, the similarly degassed IL drop was deposited on the stage and the dropcontaining liquid cell was placed again in the ultrahigh vacuum

chamber for 1 h just prior to the SEM experiment. The liquid cell, principally constructed of electrically conducting materials, was mounted and electrically grounded to the SEM to reduce specimen charging. The cell's actuator was powered by a cable run through the SEM's electrical feedthrough. After cell installation, the SEM was pumped to high vacuum, and prior to SEM imaging, the cell was visually monitored with internal cameras for 15 min to confirm specimen stability.

SEM Imaging and Data Analysis. Imaging was performed in a FEI Magellan XHR 400 FE-SEM at 3 kV acceleration voltage and 13 pA beam current, choices critical for controlling beam damage, heating, and specimen charging. The corresponding electron dose was estimated to be $\sim 10^{-3}$ e⁻ s⁻¹ Å⁻² (for comparison, the typical cryo-EM dose is ~ 10 e⁻ s⁻¹ Å⁻²). Each scan produced a 3072×2207 square pixel image, and magnification was selected such that the nominal NP diameter spanned greater than 20 pixels while individual images captured greater than 10,000 NPs. Dwell time and frame rate were optimized to minimize specimen charging and obtain proper signal-to-noise ratio. All image processing, except single particle tracking, was conducted with MATLAB 2018b. The raw grayscale images were filtered with a Gaussian blur to reduce noise and then 2D cross-correlated with an image of an isolated NP. The computed correlation displayed sharp peaks at NP centroids, and the positions of peak maxima were taken as NP positions in data analysis; these positions were determined to an accuracy of ±3 nm or better. Delaunay triangulation was performed for each particle configuration to assign NP neighbors unambiguously. The 2D pair correlation function g(r) was computed as the areal number density of NPs at center-to-center distance between r to r+dr normalized by the average NP number density across the image. NP motions were tracked using a particle-tracking toolkit, Trackpy for Python. A moderate drift in specimen position was corrected by finding the maximum in crosscorrelation between two consecutive frames.

ASSOCIATED CONTENT

Supporting Information

The Supporting Information is available free of charge at https://pubs.acs.org/doi/10.1021/acsnano.1c09853.

Description of brush-mediated NP interactions and melting of NP crystal domains; figures as described in the text (PDF)

Packing rearrangements of a jammed NP monolayer after a small stepwise area compression (<2% area change) (MP4)

Maps of several key packing metrics after interfacial compression (MP4)

NP displacements Δr accumulated over successive single time steps of duration Δt , the 18 s interval between frames (MP4)

Locally expanded 2D monolayer slowly rearranged to fill, or heal, the cavities, thereby rebalancing disparities in surface pressure (MP4)

AUTHOR INFORMATION

Corresponding Authors

David A. Hoagland – Department of Polymer Science and Engineering, University of Massachusetts Amherst, Amherst, Massachusetts 01003, United States; Email: hoagland@ mail.pse.umass.edu

Thomas P. Russell — Materials Sciences Division, Lawrence Berkeley National Laboratory, Berkeley, California 94720, United States; Department of Polymer Science and Engineering, University of Massachusetts Amherst, Amherst, Massachusetts 01003, United States; Advanced Institute for Materials Research (WPI-AIMR), Tohoku University, Sendai 980-8577, Japan; o orcid.org/0000-0001-6384-5826; Email: russell@mail.pse.umass.edu

Authors

Paul Y. Kim — Materials Sciences Division, Lawrence Berkeley National Laboratory, Berkeley, California 94720, United States; orcid.org/0000-0002-7271-0568

Yige Gao – Department of Polymer Science and Engineering, University of Massachusetts Amherst, Amherst, Massachusetts 01003, United States

Zachary Fink — Department of Polymer Science and Engineering, University of Massachusetts Amherst, Amherst, Massachusetts 01003, United States

Alexander E. Ribbe — Department of Polymer Science and Engineering, University of Massachusetts Amherst, Amherst, Massachusetts 01003, United States; orcid.org/0000-0002-9924-3429

Complete contact information is available at: https://pubs.acs.org/10.1021/acsnano.1c09853

Notes

The authors declare no competing financial interest.

ACKNOWLEDGMENTS

We acknowledge the financial support of the National Science Foundation through DMR-1807255. In depth analysis of the NP packing by PYK and TPR was supported by the U.S. Department of Energy, Office of Science, Office of Basic Energy Sciences, Materials Sciences and Engineering Division under Contract No. DE-AC02-05-CH11231 within the Adaptive Interfacial Assemblies Towards Structuring Liquids program (KCTR16).

REFERENCES

- (1) Sullivan, A. P.; Kilpatrick, P. K. The Effects of Inorganic Solid Particles on Water and Crude Oil Emulsion Stability. *Ind. Eng. Chem. Res.* **2002**, *41*, 3389–3404.
- (2) van der Sman, R. G. M.; van der Goot, A. J. The Science of Food Structuring. *Soft Matter* **2009**, *5*, 501–510.
- (3) Dinsmore, A. D.; Hsu, M. F.; Nikolaides, M. G.; Marquez, M.; Bausch, A. R.; Weitz, D. A. Colloidosomes: Selectively Permeable Capsules Composed of Colloidal Particles. *Science* **2002**, *298*, 1006–1009.
- (4) Lin, Y.; Skaff, H.; Emrick, T.; Dinsmore, A. D.; Russell, T. P. Nanoparticle Assembly and Transport at Liquid-Liquid Interfaces. *Science* **2003**, 299, 226–229.
- (5) Lin, Y.; Skaff, H.; Böker, A.; Dinsmore, A. D.; Emrick, T.; Russell, T. P. Ultrathin Cross-Linked Nanoparticle Membranes. *J. Am. Chem. Soc.* **2003**, *125*, *12690*–*12691*.
- (6) Stratford, K.; Adhikari, R.; Pagonabarraga, I.; Desplat, J.-C.; Cates, M. E. Colloidal Jamming at Interfaces: A Route to Fluid-Bicontinuous Gels. *Science* **2005**, *309*, 2198–2201.
- (7) Forth, J.; Kim, P. Y.; Xie, G.; Liu, X.; Helms, B. A.; Russell, T. P. Building Reconfigurable Devices Using Complex Liquid—Fluid Interfaces. *Adv. Mater.* **2019**, *31*, 1806370.
- (8) Balzani, V. Nanochemistry: A Chemical Approach to Nanomaterials. Geoffrey A. Ozin and André C. Arsenault. *Small* **2006**, *2*, 678–679.
- (9) Bresme, F.; Oettel, M. Nanoparticles at Fluid Interfaces. *J. Phys.: Condens. Matter* **2007**, *19*, 413101.
- (10) Montelongo, Y.; Sikdar, D.; Ma, Y.; McIntosh, A. J. S.; Velleman, L.; Kucernak; Anthony, R.; Edel, J. B.; Kornyshev, A. A. Electrotunable Nanoplasmonic Liquid Mirror. *Nat. Mater.* **2017**, *16*, 1127–1135.

- (11) Liu, X.; Kent, N.; Ceballos, A.; Streubel, R.; Jiang, Y.; Chai, Y.; Kim, P. Y.; Forth, J.; Hellman, F.; Shi, S.; Wang, D.; Helms, B. A.; Ashby, P. D.; Fischer, P.; Russell, T. P. Reconfigurable Ferromagnetic Liquid Droplets. *Science* **2019**, *365*, 264–267.
- (12) Feng, W.; Chai, Y.; Forth, J.; Ashby, P. D.; Russell, T. P.; Helms, B. A. Harnessing Liquid-in-Liquid Printing and Micropatterned Substrates to Fabricate 3-Dimensional All-Liquid Fluidic Devices. *Nat. Commun.* **2019**, *10*, 1095.
- (13) Cui, M.; Emrick, T.; Russell, T. P. Stabilizing Liquid Drops in Nonequilibrium Shapes by the Interfacial Jamming of Nanoparticles. *Science* **2013**, 342, 460–463.
- (14) Forth, J.; Liu, X.; Hasnain, J.; Toor, A.; Miszta, K.; Shi, S.; Geissler, P. L.; Emrick, T.; Helms, B. A.; Russell, T. P. Reconfigurable Printed Liquids. *Adv. Mater.* **2018**, *30*, 1707603.
- (15) Donev, A.; Torquato, S.; Stillinger, F. H.; Connelly, R. Jamming in Hard Sphere and Disk Packings. *J. Appl. Phys.* **2004**, *95*, 989–999.
- (16) Mitus, A. C.; Weber, H.; Marx, D. Local Structure Analysis of the Hard-Disk Fluid near Melting. *Phys. Rev. E* **1997**, *55*, 6855–6859.
- (17) Nelson, D. R. Bond-Orientational Order in Condensed Matter Systems; Springer: New York, 1992.
- (18) Torquato, S.; Truskett, T. M.; Debenedetti, P. G. Is Random Close Packing of Spheres Well Defined? *Phys. Rev. Lett.* **2000**, *84*, 2064–2067.
- (19) Truskett, T. M.; Torquato, S.; Sastry, S.; Debenedetti, P. G.; Stillinger, F. H. Structural Precursor to Freezing in the Hard-Disk and Hard-Sphere Systems. *Phys. Rev. E* **1998**, *58*, 3083–3088.
- (20) Aveyard, R.; Clint, J. H.; Nees, D.; Paunov, V. N. Compression and Structure of Monolayers of Charged Latex Particles at Air/Water and Octane/Water Interfaces. *Langmuir* **2000**, *16*, 1969–1979.
- (21) Chai, Y.; Lukito, A.; Jiang, Y.; Ashby, P. D.; Russell, T. P. Fine-Tuning Nanoparticle Packing at Water-Oil Interfaces Using Ionic Strength. *Nano Lett.* **2017**, *17*, 6453–6457.
- (22) Cui, M.; Miesch, C.; Kosif, I.; Nie, H.; Kim, P. Y.; Kim, H.; Emrick, T.; Russell, T. P. Transition in Dynamics as Nanoparticles Jam at the Liquid/Liquid Interface. *Nano Lett.* **2017**, *17*, 6855–6862.
- (23) Pieranski, P. Two-Dimensional Interfacial Colloidal Crystals. *Phys. Rev. Lett.* **1980**, *45*, 569–572.
- (24) Peng, Y.; Wang, Z.; Alsayed, A. M.; Yodh, A. G.; Han, Y. Melting of Colloidal Crystal Films. *Phys. Rev. Lett.* **2010**, *104*, 205703.
- (25) Rey, M.; Fernández-Rodríguez, M. A.; Steinacher, M.; Scheidegger, L.; Geisel, K.; Richtering, W.; Squires, T. M.; Isa, L. Isostructural Solid—Solid Phase Transition in Monolayers of Soft Core—Shell Particles at Fluid Interfaces: Structure and Mechanics. Soft Matter 2016, 12, 3545—3557.
- (26) Kubowicz, S.; Hartmann, M. A.; Daillant, J.; Sanyal, M. K.; Agrawal, V. V.; Blot, C.; Konovalov, O.; Möhwald, H. Gold Nanoparticles at the Liquid–Liquid Interface: X-Ray Study and Monte Carlo Simulation. *Langmuir* **2009**, *25*, 952–958.
- (27) Isa, L.; Calzolari, D. C. E.; Pontoni, D.; Gillich, T.; Nelson, A.; Zirbs, R.; Sánchez-Ferrer, A.; Mezzenga, R.; Reimhult, E. Core—Shell Nanoparticle Monolayers at Planar Liquid—Liquid Interfaces: Effects of Polymer Architecture on the Interface Microstructure. *Soft Matter* **2013**, *9*, 3789—3797.
- (28) Huerre, A.; Cacho-Nerin, F.; Poulichet, V.; Udoh, C. E.; De Corato, M.; Garbin, V. Dynamic Organization of Ligand-Grafted Nanoparticles During Adsorption and Surface Compression at Fluid–Fluid Interfaces. *Langmuir* **2018**, *34*, 1020–1028.
- (29) Schultz, D. G.; Lin, X.-M.; Li, D.; Gebhardt, J.; Meron, M.; Viccaro, J.; Lin, B. Structure, Wrinkling, and Reversibility of Langmuir Monolayers of Gold Nanoparticles. *J. Phys. Chem. B* **2006**, *110*, 24522–24529.
- (30) Costa, L.; Li-Destri, G.; Thomson, N. H.; Konovalov, O.; Pontoni, D. Real Space Imaging of Nanoparticle Assembly at Liquid—Liquid Interfaces with Nanoscale Resolution. *Nano Lett.* **2016**, *16*, 5463—5468.
- (31) Kim, P. Y.; Ribbe, A. E.; Russell, T. P.; Hoagland, D. A. Visualizing the Dynamics of Nanoparticles in Liquids by Scanning Electron Microscopy. *ACS Nano* **2016**, *10*, 6257–6264.

- (32) Crocker, J. C.; Grier, D. G. Methods of Digital Video Microscopy for Colloidal Studies. *J. Colloid Interface Sci.* **1996**, 179, 298–310.
- (33) Kaintz, A.; Baker, G.; Benesi, A.; Maroncelli, M. Solute Diffusion in Ionic Liquids, Nmr Measurements and Comparisons to Conventional Solvents. *J. Phys. Chem. B* **2013**, *117*, 11697–11708.
- (34) Wasserscheid, P.; Welton, T. *Ionic Liquids in Synthesis*; John Wiley & Sons: Weinheim, 2008.
- (35) Skrzypczak, A.; Neta, P. Diffusion-Controlled Electron-Transfer Reactions in Ionic Liquids. *J. Phys. Chem. A* **2003**, *107*, 7800–7803. (36) de Jonge, N.; Ross, F. M. Electron Microscopy of Specimens in
- Liquid. Nat. Nanotechnol. 2011, 6, 695-704. (37) Yuk, J. M.; Park, J.; Ercius, P.; Kim, K.; Hellebusch, D. J.; Crommie, M. F.; Lee, J. Y.; Zettl, A.; Alivisatos, A. P. High-Resolution
- Crommie, M. F.; Lee, J. Y.; Zettl, A.; Alivisatos, A. P. High-Resolution Em of Colloidal Nanocrystal Growth Using Graphene Liquid Cells. *Science* **2012**, *336*, 61–64.
- (38) Egerton, R. F. Control of Radiation Damage in the Tem. *Ultramicroscopy* **2013**, *127*, 100–108.
- (39) Gao, Y.; Kim, P. Y.; Hoagland, D. A.; Russell, T. P. Bidisperse Nanospheres Jammed on a Liquid Surface. ACS Nano 2020, 14, 10589–10599.
- (40) Kim, P. Y.; Gao, Y.; Chai, Y.; Ashby, P. D.; Ribbe, A. E.; Hoagland, D. A.; Russell, T. P. Assessing Pair Interaction Potentials of Nanoparticles on Liquid Interfaces. *ACS Nano* **2019**, *13*, 3075–3082.
- (41) Brandrup, J.; Immergut, E. H.; Grulke, E. A.; Abe, A.; Bloch, D. R. *Polymer Handbook*; Wiley: New York, 1999; Vol. 89.
- (42) Hansen, P. L.; Cohen, J. A.; Podgornik, R.; Parsegian, V. A. Osmotic Properties of Poly(Ethylene Glycols): Quantitative Features of Brush and Bulk Scaling Laws. *Biophys. J.* **2003**, *84*, 350–355.
- (43) Yavari, A.; Ozakin, A.; Sadik, S. Nonlinear Elasticity in a Deforming Ambient Space. *J. Nonlinear Sci.* **2016**, *26*, 1651–1692.
- (44) Tokuyama, M.; Terada, Y. How Different Is a Hard-Sphere Fluid from a Suspension of Hard-Sphere Colloids near the Glass Transition? *Phys. A: Stat. Mech. Appl.* **2007**, *375*, 18–36.
- (45) Petrov, E. P.; Schwille, P. Translational Diffusion in Lipid Membranes Beyond the Saffman-Delbrück Approximation. *Biophys. J.* **2008**, *94*, L41–L43.
- (46) Irvine, W. T. M.; Hollingsworth, A. D.; Grier, D. G.; Chaikin, P. M. Dislocation Reactions, Grain Boundaries, and Irreversibility in Two-Dimensional Lattices Using Topological Tweezers. *Proc. Natl. Acad. Sci. U.S.A.* **2013**, *110*, 15544–15548.
- (47) Kelleher, C. P.; Guerra, R. E.; Hollingsworth, A. D.; Chaikin, P. M. Phase Behavior of Charged Colloids at a Fluid Interface. *Phys. Rev. E* **2017**, *95*, 022602.
- (48) Barés, J.; Wang, D.; Wang, D.; Bertrand, T.; O'Hern, C. S.; Behringer, R. P. Local and Global Avalanches in a Two-Dimensional Sheared Granular Medium. *Phys. Rev. E* 2017, 96, 052902.
- (49) Cates, M. E.; Wittmer, J. P.; Bouchaud, J. P.; Claudin, P. Jamming, Force Chains, and Fragile Matter. *Phys. Rev. Lett.* **1998**, *81*, 1841–1844.
- (50) Heitjans, P.; Kärger, J. Diffusion in Condensed Matter: Methods, Materials, Models; Springer: New York, 2006.
- (51) Vella, D.; Aussillous, P.; Mahadevan, L. Elasticity of an Interfacial Particle Raft. *Europhys. Lett.* **2004**, *68*, 212–218.
- (52) Huang, J.; Davidovitch, B.; Santangelo, C. D.; Russell, T. P.; Menon, N. Smooth Cascade of Wrinkles at the Edge of a Floating Elastic Film. *Phys. Rev. Lett.* **2010**, *105*, 038302.
- (53) Leahy, B. D.; Pocivavsek, L.; Meron, M.; Lam, K. L.; Salas, D.; Viccaro, P. J.; Lee, K. Y. C.; Lin, B. Geometric Stability and Elastic Response of a Supported Nanoparticle Film. *Phys. Rev. Lett.* **2010**, *105*, 058301.
- (54) Lucassen, J. Dynamic Dilational Properties of Composite Surfaces. *Colloids Surf.* **1992**, *65*, 139–149.
- (55) Ethier, J. G.; Hall, L. M. Structure and Entanglement Network of Model Polymer-Grafted Nanoparticle Monolayers. *Macromolecules* **2018**, *51*, 9878–9889.